Article

A Coupled River–Overland (1D-2D) Model for Fluvial Flooding Assessment with Cellular Automata

Hsiang-Lin Yu [1,2], Tsang-Jung Chang [1,2,3,*], Chia-Ho Wang [3] and Shyh-Yuan Maa [1]

1 Department of Bioenvironmental Systems Engineering, National Taiwan University, Taipei 106, Taiwan; andy780421@gmail.com (H.-L.Y.); r07622026@ntu.edu.tw (S.-Y.M.)
2 Hydrotech Research Institute, National Taiwan University, Taipei 106, Taiwan
3 Center for Weather and Climate Disaster Research, National Taiwan University, Taipei 106, Taiwan; wangchiaho@ntu.edu.tw
* Correspondence: tjchang@ntu.edu.tw

Abstract: To provide accurate and efficient forecasting of fluvial flooding assessment in the river basin, the present study links the well-known CA-based urban inundation modeling (2D-OFM-CA) with a one-dimensional river flow model (1D-RFM) as a coupled 1D-2D river–overland modeling. Rules to delineate the geometric linking between the 1D-RFM and 2D-OFM-CA along embankments are developed. The corresponding exchanged water volume across an embankment is then computed by using the free and submerged weir flow formulas. The applicability of the proposed coupled model on fluvial flooding assessment is then assessed and compared with a well-recognized commercial software (HEC-RAS model) through an idealized fluvial case and an extensively studied real-scale fluvial case in the Severn River Basin. Based on the simulated results concerning the numerical accuracy, the coupled model is found to give similar results in the aspects of the river flow and overland flow modeling in both two study cases, which demonstrates the effectiveness of the linking methodology between the 1D-RFM and 2D-OFM-CA. From the viewpoint of numerical efficiency, the coupled model is 47% and 41% faster than the HEC-RAS model in the two cases, respectively. The above results indicate that the coupled model can reach almost the same accuracy as the HEC-RAS model with an obvious reduction in its computational time. Hence, it is concluded that the coupled model has considerable potential to be an effective alternative for fluvial flooding assessment in the river basin.

Keywords: unsteady river flow; 2D flood inundation model; cellular automata; coupled model; levee overtopping

1. Introduction

Flooding is recognized to be a highly destructive natural event that could cause tremendous loss of money and human lives. Generally, there are pluvial and fluvial floodings, depending on the causes of the flooding. For fluvial flooding, the water levels in rivers are raised above the elevations of levees because of massive upstream inflows, which subsequently cause overtopping discharges into neighboring lands. The overtopping discharges can not only breach levees, such that more overtopping discharges are introduced into lands, but also destroy buildings and other facilities in the lands because of the high momentum carried. For example, in the Katrina hurricane on 27–29 August 2005, levees were breached because of very high water discharges and consequently caused very severe fluvial flooding in New Orleans. On 5–7 July 2020, a very heavy rainfall event with a precipitation amount of 1599 mm in the Kumamoto prefecture of Japan caused the mainstream to seriously swell and subsequently breach the levees such that there are many lives lost in the resultant massive fluvial floods. Later, in July 2022, the greater Sydney area encountered severe fluvial flooding due to a frontal precipitation system that dumped 800 mm of rainfall in New South Wales within only four days. Later, in April 2024, more than 100 cities in

the Rio Grande do Sul state in Brazil faced an extreme rainfall event. Very severe floods and mudflows damaged bridges, buildings, roads, and dams and caused enormous loss of money and lives. Hence, to mitigate the great losses due to fluvial flooding, it is essential to build an accurate and efficient tool to predict the potential fluvial flooding before the actual flooding occurs [1].

Basically, fluvial flooding modeling involves the simulations of the water bodies in the river and ground surface and the bidirectional transports of water between them. Correspondingly, it requires 1D river flow modeling, two-dimensional (2D) overland flow modeling, and an appropriate 1D-2D dynamic linking to form the coupled model for fluvial flooding modeling. Specifically, in terms of the 1D-2D linking, there are models that only consider the mass exchanging by using the free/submerge weir formulas under the assumption that the approaching velocities toward the weir can be ignored [2–6] and models that consider both the mass and momentum exchanging [7–9]. So far, there have been various sophisticated commercial programs with well-recognized accuracy and satisfactory efficiency for fluvial flood modeling, for example, the HEC-RAS model [10], Infowork ICM [11], and Mike Flood [12], etc. These coupled models often adopt the river flow models (RFMs) that numerically solve the de Saint Venant equations [13] for river flow modeling and the overland flow models (OFMs) that numerically solve the full 2D shallow water equations (2D-SWEs) [14–22]. Nevertheless, in spite of their recognized accuracy and satisfactory efficiency [6,23], these coupled models are still reported to be time-consuming because of the heavy numerical operators from their OFMs [24], especially in large-scale applications [20,22]. To resolve this issue, many researchers worked to increase the efficiency of their OFMs. As summarized by Jamali et al. (2018) [25], the attempts to increase the efficiency of OFMs can be classified into three categories: detail reduction, maximum use of computational resources, and model simplification. For the detail reduction category, less detailed data or bigger time steps are used to increase efficiency [26]. As to the maximum use of computational resources, parallel computing or code parallelization is implemented [27,28]. There are various approaches to the model simplification category. Some researchers built their models by solving the simplified 2D shallow water equations that ignore the local acceleration term and/or convective acceleration term of the full dynamic-wave equations, e.g., Bates et al. [12] and Caviedes-Voullième et al. [29]. Some researchers built highly conceptual models to simulate overland flows [30,31]. Also, some researchers see the overland flow movement as the combination of surface depressions and overland flow paths to build their 1D-1D overland flow models [25,32].

In addition to these approaches in the model simplification category, some researchers turned to utilizing the Cellular Automata (CA) framework to build their efficient models. In the CA framework, the computational domain is seen as a set of discretized computational cells with the same shape [33]. Each computational cell is assigned a state to represent the considered physics [34]. The state of each computational cell is explicitly evolved by a set of generic transition rules that involve states of the computational cell and its predefined neighbor cells [35]. Thus, simple algebraic equations can be used to simulate the considered physics without the need to incorporate tedious numerical operators [36], which contributes to the remarkable efficiency of the CA framework. Also, the CA framework is inherently prone to parallel computing [36]. Aiming to benefit from the CA framework, various CA-based OFMs have been built, e.g., the CA flood inundation model by Dottori and Todini [37], the CA2D model by Ghimire et al. [38], the flood routing model by Cai et al. [39], the WCA2D model by Guidolin et al. [40], the OFS-CA model by Jahanbazi et al. [41], the CA-ffé model by Jamali et al. (2019) [42], the 2DCA by Tavakolifar et al. [43], and the SWFCA model by Chang et al. [24]. As summarized by Chang et al. [24], most of these CA-based OFMs use water levels as the key to determining wave movements based on the assumption that the water movement goes from a high water level to a low water level. As a result, these CA-based OFMs behave like a non-inertia wave approximation [44] and are found to efficiently provide accurate enough results in simulating regular flows. In terms of the strong discontinuous flows, including transcritical flows (hydraulic jumps/drops) and wet–dry interfaces where inertia becomes crucial, they become inaccurate and even more time-

consuming [24]. Although such a limitation is resolved by using the Bernoulli hydraulic head to delineate water movement in the SWFCA model of Chang et al. [24], it is still found that when most of the flows are regular flows, the non-inertia CA-based model (i.e., the WCA2D model) can still provide almost the same accurate result in a significantly reduced run time [24]. Also, because of its recognized accuracy and remarkable efficiency, the WCA2D model has further been combined with other models in various applications, e.g., water quality [45] and as the 2D-OFM-CA in urban inundation modeling [46]. Nevertheless, this CA-based OFM (2D-OFM-CA) has not been connected with a river flow model as a fluvial flood assessment tool that can benefit from the remarkable efficiency improvement of the CA framework on the overland flow modeling.

Hence, the present study couples the 2D-OFM-CA with a sophisticated 1D river flow model as a novel river–overland (1D-2D) modeling for fluvial flooding assessment. Rules are incorporated to delineate the geometric linking and compute the exchanged water volume between the 1D-RFM and 2D-OFM-CA. To discover whether the proposed coupled model can be an effective alternative for fluvial flood assessment, the HEC-RAS model, having well-recognized high accuracy and efficiency in fluvial flood modeling, is selected among various coupled models to conduct the evaluation through two fluvial study cases. Focus is devoted to discovering how fast the coupled model can achieve without losing the required accuracy.

2. Coupled River–Overland (1D-2D) Modeling with Cellular Automata

The coupled model consists of three components: the 1D river flow model, the 2D overland flow model, and the 1D-2D dynamic interaction between them. Their details are introduced as follows.

2.1. D River Flow Model (1D-RFM)

The utilized 1D-RFM by Hsu et al. [47] is built under the assumption that the dimension along the river line is much longer than the dimension perpendicular to the river line. The governing equations of the used 1D-RFM are de Saint Venant equations, which consist of the continuity and momentum equations as

$$\frac{\partial Q}{\partial x} + \frac{\partial A}{\partial t} - q_{r(in)} + q_{r(out)} = 0 \tag{1}$$

$$\frac{\partial Q}{\partial t} + \frac{\partial}{\partial x}\left(\frac{Q^2}{A}\right) - gA\left(S_0 - \frac{\partial h}{\partial x} - S_f\right) - q_{r(in)}v_{r(in)} + q_{r(out)}v_{r(out)} = 0 \tag{2}$$

in which A is the cross-sectional area, g is the gravitational acceleration, h is the water level, Q is the water discharge, $q_{r(in)}$ is the lateral inflow per river segment, $q_{r(out)}$ is the lateral outflow per river segment, $v_{r(in)}$ is the average water velocity of the lateral inflow along the flow direction of the river, $v_{r(out)}$ is the average water velocity of the lateral outflow along the flow direction of the river, S_0 is the bed friction slope, and S_f is the friction loss slope. In the 1D-RFM, the friction loss slope S_f is expressed as

$$S_f = \frac{n^2 Q|Q|}{A^2 R^{4/3}} \tag{3}$$

where n is the Manning roughness coefficient and R is the hydraulic radius. It is worth mentioning that, due to the use of the de Saint Venant equations, the 1D-RFM cannot simulate the change in the perpendicular direction, for example, the water depth change in a bending channel due to the secondary flow. In spite of this limitation, the 1D-RFM can still accurately simulate a river system. In the 1D-RFM, Equations (1) and (2) are numerically solved by the non-linear fully implicit finite difference method. The time and spatial derivatives in the continuity and momentum equations are expressed as follows:

$$f_j = \frac{1}{2}\left(f_{j+1}^{t+\Delta t_{RFM}} + f_j^{t+\Delta t_{RFM}}\right) \tag{4}$$

$$\frac{\partial f_j}{\partial t} = \frac{1}{2\Delta t_{RFM}}\left[\left(f_{j+1}^{t+\Delta t_{RFM}} - f_{j+1}^t\right) + \left(f_j^{t+\Delta t_{RFM}} - f_j^t\right)\right] \tag{5}$$

$$\frac{\partial f_j}{\partial x} = \frac{1}{\Delta x_{j\to j+1,(RFM)}}\left(f_{j+1}^{t+\Delta t_{RFM}} - f_j^{t+\Delta t_{RFM}}\right) \tag{6}$$

In Equations (4)–(6), the subscript j represents the j cross-section, f_j refers to the water discharge or water depth at the j cross-section, Δt_{RFM} is the adaptive time step of this river flow model, and $\Delta x_{j\to j+1,(RFM)}$ is the distance between j and $j + 1$ cross-sections. Substituting Equations (4)–(6) into Equations (1) and (2), the continuity and momentum equations between the subsequent two cross-sections can be arranged to be the functions of the water discharge and depth as

$$C_j\left(Q_{j+1,(RFM)}^{t+\Delta t_{RFM}}, h_{j+1,(RFM)}^{t+\Delta t_{RFM}}, Q_{j,(RFM)}^{t+\Delta t_{RFM}}, h_{j,(RFM)}^{t+\Delta t_{RFM}}, Q_{j+1,(RFM)}^t, h_{j+1,(RFM)}^t, Q_{j,(RFM)}^t, h_{j,(RFM)}^t\right) = 0 \tag{7}$$

$$M_j\left(Q_{j+1,(RFM)}^{t+\Delta t_{RFM}}, h_{j+1,(RFM)}^{t+\Delta t_{RFM}}, Q_{j,(RFM)}^{t+\Delta t_{RFM}}, h_{j,(RFM)}^{t+\Delta t_{RFM}}, Q_{j+1,(RFM)}^t, h_{j+1,(RFM)}^t, Q_{j,(RFM)}^t, h_{j,(RFM)}^t\right) = 0 \tag{8}$$

where C_j and M_j are, respectively, the differenced continuity and momentum equations between the j and $j + 1$ cross-sections. Based on the prescribed boundary and initial conditions, the Newton–Raphson method iteratively finds the solutions of Equations (7) and (8). For more details, the readers are referred to Hsu et al. [47].

2.2. CA-Based 2D Overland Flow Model (2D-OFM-CA)

The present study utilizes the 2D-OFM-CA developed by Guildolin et al. [40] and modified by Chang et al. [46] to simulate surface runoffs in an accurate enough and efficient way. In the 2D-OFM-CA, the computational domain is discretized based on the Cartesian square cell because of the simplicity of programming. As for the neighborhood configuration that defines the involved surrounding cells in evolving the state of a cell, the von Neumann neighborhood configuration is selected. Based on the assumption that the water movement goes from a high water level to a low water level, the water level is selected as the state of each computational cell. Also, the water level is used as the key to decide the transported direction from the central cell to its four surrounding von Neumann neighbor cells. The subsequent intercellular volume from a computational cell to one of its neighbor cells is determined by using the Manning and critical flow equations. Thus, the 2D-OFM-CA behaves like the non-inertia wave approximation [40,46]. To further lower the involved computational demands in deciding the intercellular volume, a local weight system that uses the available volume as the weight is incorporated, which can also ensure mass conservation.

First, in delineating the water movement, the water level difference between the central cell and its ith neighbor cell ($\Delta h_{0,i,(OFM)}$) is computed as

$$\Delta h_{0,i,(OFM)} = \max\left(h_{0,(OFM)} - h_{i,(OFM)}, 0\right) \forall i \in \{1\ldots 4\} \tag{9}$$

in which the subscript i represents the ith neighbor cell and $h_{0,(OFM)}$ and $h_{i,(OFM)}$ refer to the water levels of the central cell and ith neighbor cell, respectively. Next, the available volume of the ith neighbor cell ($\Delta V_{0,i,(OFM)}$) is computed as

$$\Delta V_{0,i,(OFM)} = \begin{cases} L_{OFM}^2 \Delta h_{0,i,(OFM)} & \Delta h_{0,i,(OFM)} > \tau_{OFM} \\ 0 & \Delta h_{0,i,(OFM)} \leq \tau_{OFM} \end{cases} \tag{10}$$

where τ_{OFM} is the water level difference tolerance to define whether the water level difference is large enough to have a flow sent from the central cell to this neighbor cell. In Equation (10), L_{OFM} is the length of the square cell. For the central cell with all available volumes equal to zero, the determination of intercellular volume is performed, and the

following processes are escaped. Otherwise, the available volume is used to compute the weights of the central cell ($w_{0,(OFM)}$) and ith neighbor cell ($w_{i,(OFM)}$) as

$$w_{0,(OFM)} = \frac{\Delta V_{\min,(OFM)}}{\Delta V_{tot,(OFM)} + \Delta V_{\min,(OFM)}} \tag{11}$$

$$w_{i,(OFM)} = \frac{\Delta V_{0,i,(OFM)}}{\Delta V_{tot,(OFM)} + \Delta V_{\min,(OFM)}} \quad \forall i \in \{1 \ldots 4\} \tag{12}$$

where $\Delta V_{\min,(OFM)}$ is the minimum value among the non-zero available volumes, $\Delta V_{\max,(OFM)}$ is the maximum value among the available volumes, and $\Delta V_{tot,(OFM)}$ is the sum of the available volumes. After the weights are determined, the 2D-OFM-CA then decides the total intercellular volume that is sent from the central cell to its neighbor cells ($I_{tot,(OFM)}^{t+\Delta t_{OFM}}$) as

$$I_{tot,(OFM)}^{t+\Delta t_{OFM}} = \min\left(d_{0,(OFM)}L_{OFM}^2, \frac{I_{\mathbf{M},(OFM)}}{w_{\mathbf{M},(OFM)}}, \Delta V_{\min,(OFM)} + I_{tot,(OFM)}\right) \tag{13}$$

where $d_{0,(OFM)}$ is the water depth of the central cell, $w_{\mathbf{M},(OFM)}$ is the largest weight among the four neighbor cells, $I_{\mathbf{M},(OFM)}$ is the intercellular volume of the **M**th neighbor cell with the largest weight, $I_{tot,(OFM)}$ is the total intercellular volume leaving the central cell at the previous time step, and Δt_{OFM} is the adaptive time step of the 2D-OFM-CA. In Equation (13), $d_{0,(OFM)}L_{OFM}^2$ is the water volume of the central cell and is used to ensure mass conservation and $I_{\mathbf{M},(OFM)}/w_{\mathbf{M},(OFM)}$ is the total intercellular volume derived based on the local weight system. Within the third term of Equation (13), $\Delta V_{\min,(OFM)}$ is used to prevent artificial oscillations between the central cell and its neighbor cells. As for $I_{tot,(OFM)}$, it is incorporated to avoid significant change between two subsequent time steps. $I_{\mathbf{M},(OFM)}$ in Equation (13) is computed as

$$I_{\mathbf{M},(OFM)} = v_{\mathbf{M},(OFM)}d_{0,(OFM)}L_{OFM}\Delta t_{OFM} \tag{14}$$

with $V_{\mathbf{M},(OFM)}$ as the intercellular velocity computed by the Manning and critical flow equations

$$V_{\mathbf{M},(OFM)} = \min\left(\sqrt{gd_{0,(OFM)}}, \frac{1}{n_{0,(OFM)}}d_{0,(OFM)}^{\frac{2}{3}}\sqrt{\frac{\Delta h_{0,\mathbf{M},(OFM)}}{L_{OFM}}}\right) \tag{15}$$

in which $n_{0,(OFM)}$ is the Manning roughness of the central cell.

After the total intercellular is computed by Equation (13), the intercellular volume to the ith neighbor cell is given as

$$I_{i,(OFM)}^{t+\Delta t_{OFM}} = I_{tot,(OFM)}^{t+\Delta t_{OFM}} \times w_{i,(OFM)} \tag{16}$$

Then, when all computational cells have decided their intercellular volumes, the water depth of each computational cell ($d_{0,(OFM)}^{t+\Delta t_{OFM}}$) is updated by

$$d_{0,(OFM)}^{t+\Delta t_{OFM}} = d_{0,(OFM)} - \frac{\sum_{i=1}^{4} I_{i,(OFM)}^{t+\Delta t_{OFM}}}{L_{OFM}^2} + \frac{\Delta V_{0,(OFM)}^{in}}{L_{OFM}^2} - \frac{\Delta V_{0,(OFM)}^{out}}{L_{OFM}^2} \tag{17}$$

where $\Delta V_{0,(OFM)}^{in}$ refers to the input water volume to the central cell, including precipitation, transported water from the upstream cells, inflows from the upstream catchments, and overflows from rivers. It is worth mentioning that the 2D-OFM-CA handles the rainfall–runoff process by sending rainfall through $\Delta V_{0,(OFM)}^{in}$ in Equation (17) and computing the

resultant runoffs by Equations (9)–(16). As to $\Delta V_{0,(OFM)}^{out}$, it is the lost water volume from the central cell, including infiltration, lateral outflows, and inflow to rivers.

Finally, in terms of the adaptive time step Δt_{OFM}, the 2D-OFM-CA utilizes the CFL and diffusion stability conditions [48] to decide its value. Specifically, concerning the adaptive time step computed under the diffusion stability condition, the 2D-OFM-CA sets up a so-called slope tolerance σ_{OFM} to exclude the computation of the adaptive time step when the water surface difference tends to zero. Moreover, since huge computational demands are involved in finding the new adaptive time step by the formulas of the CFL and diffusion stability conditions, the 2D-OFM-CA incorporates the use of the update time step $\Delta t_{u,(OFM)}$ such that the new value of the adaptive time step is only computed at specific time stamps ($t = K\Delta t_{u,(OFM)}, K = 1, 2, \ldots$). For other details, the readers are referred to Guidolin et al. [40] and Chang et al. [46].

2.3. The Dynamic Interaction between the 1D-RFM and 2D-OFM-CA

The adopted 1D-RFM originally had its own method for computing linear source overtopping discharges. Nevertheless, to increase the simplicity of programming for linking the 1D-RFM and 2D-OFM-CA, the mechanism to compute the overtopping discharges in the 1D-RFM is discarded. Instead, the present study proposes a new linking methodology to exchange the water between the two models. For the 1D-RFM, overtopping discharges can be sent into the 2D-OFM-CA along the left and right embankments of a river segment between two subsequent cross-sections. For the 2D-OFM-CA, the computational cells that are near the embankments are marked to be the *river cells* that will receive overtopping discharges from the 1D-RFM or send lateral surface runoffs to the 1D-RFM. The details for the geometric linking methodology and computations of exchanged discharges (overtopping discharges/lateral surface runoffs) are described in the following Sections 2.3.1 and 2.3.2. As for the time synchronization between the 1D-RFM and 2D-OFM-CA, it is introduced in Section 2.3.3.

2.3.1. Geometric Linking Methodology

Usually, the spatial resolution of the 1D-RFM is larger than the 2D-OFM-CA, i.e., $\Delta x_{j \to j+1,(RFM)} > L_{OFM}$. Hence, there will be more than one river cell in a left/right embankment of a river segment. On the other hand, in terms of the reorganization of river cells, firstly, the left and right embankment line features and the cross-section point feature in the 1D-RFM are utilized to derive the left/right embankment lines of each river segment. Then, for an embankment in a river segment, the corresponding line feature is used to select the contained river cells. For a river cell that is not located at the start or end of the embankment, it will be recognized to be within this embankment. As for the river cell that is located at the start or end of the embankment, only the river cell at the end of the embankment will be judged to be within this embankment. Thus, after delineation, an embankment will have P_b river cells. The above delineation strategy is illustrated in Figure 1. Taking the right embankment in the river segment between the j and $j + 1$ cross-sections for example (the line that is marked as the actual right bank in Figure 1), there are nine river cells that will exchange water with this embankment. It is noted that, in this 1D-2D dynamic linking methodology, the right bank between the cross-sections j and $j + 1$ is hereinafter represented by the river cells, as displayed as the purple line with a mark as "digitalized right bank" in Figure 1.
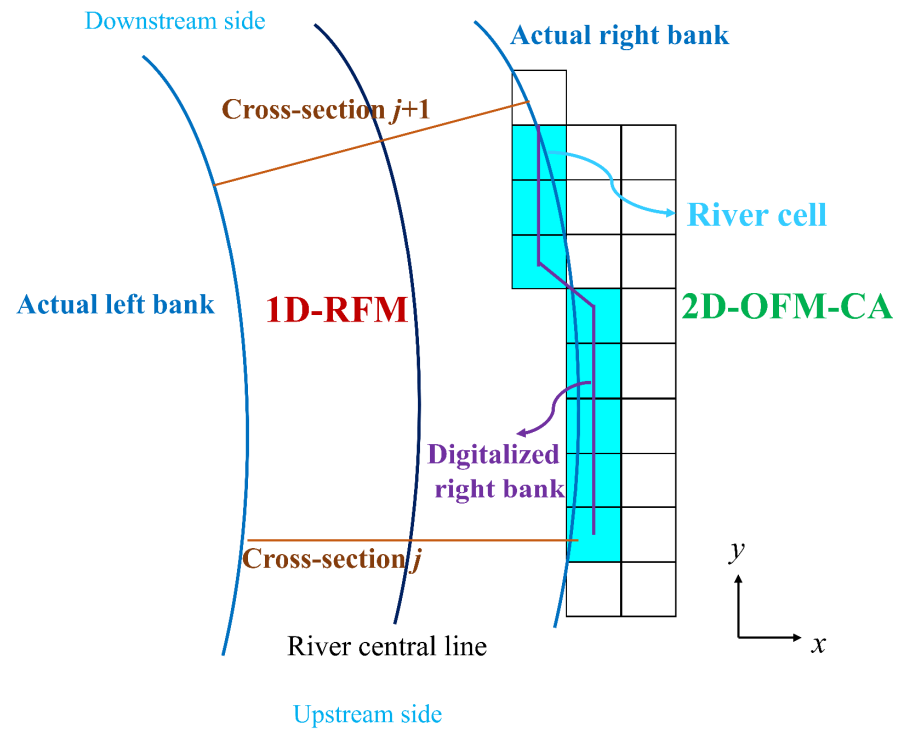
Figure 1. The schematic illustration of the geometric linking methodology between the 1D-RFM and 2D-OFM-CA.

2.3.2. Exchanged Discharge Computation

The present study considers the overtopping discharges from the 1D-RFM to the 2D-OFM and the lateral surface runoffs from the 2D-OFM-CA to the 1D-RFM according to the relative relation among the water levels in the river segment, water levels of the corresponding river cells, and elevations along the embankment. For simplicity, the present study uses the average water level of the river segment, the average water level of the corresponding river cells, and the average elevation of the embankment for computation. The average water level of the river segment ($\bar{h}_{j \to j+1,(RFM)}$) is determined as

$$\bar{h}_{j \to j+1,(RFM)} = \frac{\left(h_{j,(RFM)} + z_{j,(RFM)}\right) + \left(h_{j+1,(RFM)} + z_{j+1,(RFM)}\right)}{2} \tag{18}$$

in which $z_{j,(RFM)}$ and $z_{j+1,(RFM)}$ are the bottom elevations of the j and $j+1$ cross-sections in the 1D-RFM, respectively. Then, for an embankment of the river segment, for example, the right embankment in Figure 1, the average elevation of the right embankment ($\bar{z}_{j \to j+1,REB}$) is given as

$$\bar{z}_{j \to j+1,REB} = \frac{1}{P_b} \sum_{k=1}^{P_b} \hat{z}_{j \to j+1,REB,k} \tag{19}$$

in which subscript *REB* refers to the right embankment, subscript k refers to contained river cells of the embankment, and $\hat{z}_{j \to j+1,REB,k}$ is the given embankment elevation of the kth river cell within this right embankment in this river segment. In the present study, $\hat{z}_{j \to j+1,REB,k}$ is computed by taking the investigated data of this right embankment (location, height) with linear interpolation. The average water level of the contained river cells of this right embankment ($\bar{h}_{j \to j+1,REB,(OFM)}$) is computed by

$$\bar{h}_{j \to j+1,REB,(OFM)} = \frac{1}{P_b} \sum_{k=1}^{P_b} h_{j \to j+1,REB,k,(OFM)} \tag{20}$$

In the above equation, $h_{j\to j+1,REB,k,(OFM)}$ is the water level of the kth river cell within this right embankment. Next, based on $\overline{h}_{j\to j+1,(RFM)}$ and $\overline{h}_{j\to j+1,REB,(OFM)}$, the coupled method computes either the overtopping discharges or lateral surface runoffs, which are discussed as follows.

1. Computation of the overtopping discharges from the 1D-RFM to the 2D-OFM-CA

For an embankment (e.g., the right embankment in Figure 1) in a river segment, when the average water level of the river segment ($\overline{h}_{j\to j+1,(RFM)}$) is larger than the average water level of the contained river cells ($\overline{h}_{j\to j+1,REB,(OFM)}$), the 1D-RFM can send overtopping discharge to the corresponding river cells in the 2D-OFM-CA. The overtopping discharge of the right embankment ($Q_{OT,j\to j+1,REB}$) is computed by using the free or sub-merged weir equations as

$$
Q_{OT,j\to j+1,REB} = \begin{cases} 0 & \text{if } \overline{h}_{j\to j+1,(RFM)} \leq \overline{z}_{j\to j+1,REB} \\ \frac{2}{3}\mu_{OT}C_d L \sqrt{2g}\left(\Delta\overline{h}_{OT}\right)^{1.5} & \text{if } \overline{h}_{j\to j+1,(RFM)} > \overline{z}_{j\to j+1,REB} \end{cases} \tag{21}
$$

$$
\mu_{OT} = \begin{cases} 1.0 & \text{if } \overline{h}_{j\to j+1,REB,(OFM)} \leq \overline{z}_{j\to j+1,REB} \\ \left[1 - \left(\frac{\overline{h}_{j\to j+1,REB,(OFM)}-\overline{z}_{j\to j+1,REB}}{\overline{h}_{j\to j+1,(RFM)}-\overline{z}_{j\to j+1,REB}}\right)^{1.5}\right]^{0.385} & \text{if } \overline{h}_{j\to j+1,REB,(OFM)} > \overline{z}_{j\to j+1,REB} \end{cases} \tag{22}
$$

in which the subscript OT refers to the overtopping discharge, C_d is the weir coefficient, L is the length of this right embankment, and $\Delta\overline{h}_{OT} = \overline{h}_{j\to j+1,(RFM)} - \overline{h}_{j\to j+1,REB,(OFM)}$. The contained river cells receive an average overtopping discharge ($\overline{Q}_{OT,j\to j+1,REB}$) as

$$
\overline{Q}_{OT,j\to j+1,REB} = \frac{1}{P_b}Q_{OT,j\to j+1,REB} \tag{23}
$$

2. Computation of the lateral surface runoffs from the 2D-OFM-CA to the 1D-RFM

River cells can send lateral surface runoffs to the 1D-RFM when the corresponding embankment does not send overtopping discharges to the river cells. The corresponding lateral surface runoff for a river cell ($Q_{LI,j\to j+1,REB,k}$) is computed by

$$
Q_{LI,j\to j+1,REB,k} = \begin{cases} 0 & \text{if } h_{j\to j+1,REB,k,(OFM)} \leq \hat{z}_{j\to j+1,REB,k} \\ \frac{2}{3}\mu_{LI}C_d L_{j\to j+1,REB,k}\sqrt{2g}(\Delta h_{LI})^{1.5} & \text{if } h_{j\to j+1,REB,k,(OFM)} > \hat{z}_{j\to j+1,REB,k} \end{cases} \tag{24}
$$

$$
\mu_{LI} = \begin{cases} 1.0 & \text{if } \hat{h}_{j\to j+1,REB,k,(RFM)} \leq \hat{z}_{j\to j+1,REB,k} \\ \left[1 - \left(\frac{\hat{h}_{j\to j+1,REB,k,(RFM)}-\hat{z}_{j\to j+1,REB,k}}{h_{j\to j+1,REB,k,(OFM)}-\hat{z}_{j\to j+1,REB,k}}\right)^{1.5}\right]^{0.385} & \text{if } \hat{h}_{j\to j+1,REB,k,(RFM)} > \hat{z}_{j\to j+1,REB,k} \end{cases} \tag{25}
$$

in which the subscript LI refers to the lateral surface runoffs, $L_{j\to j+1,REB,k}$ is the length of the right embankment within the kth river cell, $\hat{h}_{j\to j+1,REB,k,(RFM)}$ is the interpolated water level of the kth river cell from the water levels of the j and $j + 1$ cross-sections in the 1D-RFM by the linear interpolation, and $\Delta h_{LI} = h_{j\to j+1,REB,k,(OFM)} - \hat{z}_{j\to j+1,REB,k}$. For the considered embankment, the lateral surface runoffs of the P_b river cells will be summed as the total lateral inflow $Q_{LI,j\to j+1,REB}$ as

$$
Q_{LI,j\to j+1,REB} = \sum_{k=1}^{P_b} Q_{LI,j\to j+1,REB,k} \tag{26}
$$

The exchanged discharges of the left embankment of this considered river segment can be simulated in the same manner.

2.3.3. Time Synchronization between the 1D-RFM and 2D-OFM-CA

It is reported that the 1D-RFM can use large adaptive time steps of up to one hour to perform simulations because of the use of an implicit scheme in the 1D-RFM. Hence, in this proposed coupled model, the 1D-RFM and 2D-OFM-CA both use the adaptive time step of the 2D-OFM-CA (Δt_{OFM}) to perform their corresponding simulations and the two models exchange water at each time step.

As for the water exchanging between the 1D-RFM and 2D-OFM-CA, for a river cell in the 2D-OFM-CA, the overtopping discharge from the 1D-RFM to this cell is multiplied by the adaptive time step and added into $\Delta V^{in}_{0,(OFM)}$ in Equation (17). Conversely, the lateral surface runoff from the river cell to the corresponding embankment in the river segment is multiplied with the adaptive time step and added to $\Delta V^{out}_{0,(OFM)}$ in Equation (17). As for a river segment in the 1D-RFM, the received lateral surface runoffs from its two embankments are multiplied by the adaptive time step and added to the 1D-RFM through the continuity equation (Equation (7)). Similarly, the overtopping discharges from the river segment are summed and multiplied by the adaptive time step and subtracted from the 1D-RFM through the continuity equation. It is noted that, for the 1D-RFM, the aforementioned sent volume to the 2D-OFM-CA and received volume from the 2D-OFM-CA are both assumed to have no influence on the momentum equation (Equation (8)).

3. Model Verification

In this section, the accuracy and efficiency of the proposed coupled model are evaluated and compared with the HEC-RAS model (version 5.0.7) through an idealized study case. Briefly speaking, it simulates 1D river flows by using the Preissmann four-point implicit finite difference method to solve de Saint Venant equations. As to 2D overland flow modeling, the HEC-RAS model adopts the finite volume method (FVM) to discretize 2D shallow water equations on the unstructured grid system. In terms of the linkage between the 1D and 2D modules in the HEC-RAS model, the exchanged water volume along an embankment is computed by modified free and submerged weir formulas that include the consideration of the spatial variations of water surface and embankment elevation [10,49].

3.1. Case Delineation

The idealized case comprises a straight 4100 m-long river and two 1000 m × 1000 m square plates (Floodplains A and B in Figure 2a). The bed slopes of the river, Floodplain A and Floodplain B, are 0.001, 0.001, and 0, respectively, as illustrated in Figure 2a. It is worth mentioning that the slopes of Floodplains A and B are designed to make the resultant overland flows have a large portion of regular flows. As to the river system, the cross-section of the river has a width of 10 m and a height of 10 m, as depicted in Figure 2a. Floodplain A is located upstream of the river and connects to the right bank of the river. As for Floodplain B, it connects to the bottom of the right bank at the downstream side of the river. To verify the proposed linking methodology of the present study, Floodplain A is designed to introduce lateral surface runoffs into the river because of uniform distributed rainfall. As to Floodplain B, it is placed to receive overtopping discharges from the 1000 m × 5.95 m opening at the right bank of the river.

In terms of the grid resolution of the computational domain, the accuracy and efficiency of a coupled model for fluvial flood assessment (i.e., the proposed coupled model and the HEC-RAS model) have a direct relation with the adopted 2D overland flow modeling. Concerning the proposed coupled model, since the used 2D-OFM-CA behaves like the non-inertia wave approximation [24], the relation between its accuracy/efficiency with the grid resolution is similar to other non-inertia models. As studied by Caviedes-Voullième et al. [29], the accuracy of a non-inertia model is less sensitive to the grid resolution than its dynamic-wave alternative. Additionally, it is found that when the grid resolution becomes finer, the accuracy of the non-inertia model becomes less, whereas its dynamic-wave alternative becomes higher. The non-inertia wave model might perform better than its dynamic-wave alternative under a not-too-coarse grid resolution due to the numerical issue

caused by the numerical viscosity of the dynamic-wave alternative. On the other hand, when the grid resolution becomes finer, the efficiency of the non-inertia model becomes less than its dynamic-wave alternative due to the use of relatively smaller time steps of the non-inertia model to maintain its stability. Thus, to simultaneously let the coupled model be able to have accurate enough results with obviously improved efficiency, a square cell with a length of 10 m is used to discretize the two floodplains into 20,000 square cells. The Manning roughness coefficients of the river and two floodplains are 0.02 $s/m^{1/3}$ and 0.05 $s/m^{1/3}$, respectively. The river is discretized into 42 equal-sized cross-sections in an equal interval of 100 m. A fixed inflow discharge of 5 m^3/s is prescribed at the upstream edge of the river. At the downstream end of the river, a fixed water depth of 4 m is given to introduce sub-critical flows such that the changes in water level and discharge in the river are majorly attributed to the lateral surface runoffs from Floodplain A. Initially, the two floodplains are both dry and have all their edges closed except for the edges on the right bank of the river. The prescribed uniform rainfall on Floodplain A has a duration of 2 h, and a peak rainfall intensity of 30 mm/15 min, as drawn in Figure 2b. The simulation duration of this idealized study case is 6 h to discover the climbing and falling limbs in the river. Both the coupled and HEC-RAS models are built following their manuals [40,49]. Specifically, for the coupled model, the model parameters of the 2D-OFM-CA (e.g., water level difference tolerance, slope tolerance, update time step, etc.) are assigned with the suggested values of the manual for the purpose of demonstration [40]. For the HEC-RAS model, rectangular cells are used to delineate the computational domain. The resultant simulations are conducted on a personal computer equipped with Intel® Core™ i9-9900K CPU with 16 GB RAM (DDR4).
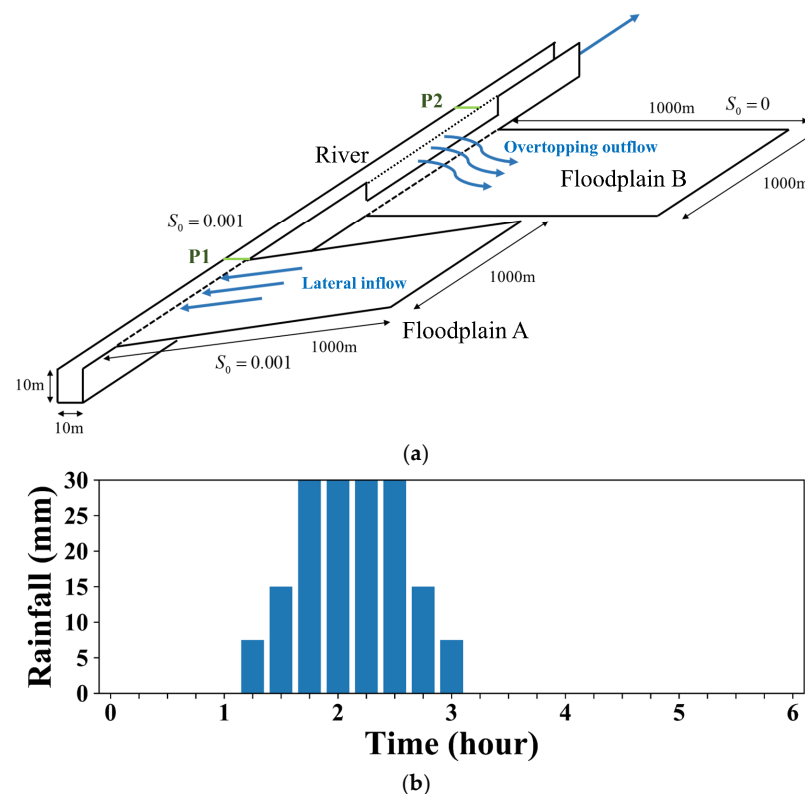

(a)

(b)

Figure 2. (**a**) The configuration of the idealized study case. The locations of the two measured stations in the river for inspecting water level and discharge hydrographs are plotted in the figure as well. (**b**) The input rainfall data on Floodplain A that introduces lateral surface runoffs into the river and subsequently causes overtopping discharges to Floodplain B.

The accuracy of the coupled model in 1D river flow modeling is verified by comparing the simulated water level and discharge hydrographs of the two models at two measured

stations (i.e., P1 and P2, as depicted in Figure 2a). The Nash–Sutcliffe Efficiency (NSE) by Nash and Sutcliffe [50] and the Mean Square Error (MSE) of the coupled model are computed by using the results of the HEC-RAS model as the exact solutions to quantify the accuracy of the coupled model. Moreover, the accuracy of the coupled model is also assessed by conducting a peak error analysis on the water level peak and arrival time of the peak.

3.2. Accuracy Verification and Efficiency Assessment

The accuracy comparison is conducted by comparing the results in the river flow modeling and overland flow modeling. Concerning the river flow modeling, the comparison is taken at the two cross-sections in the river where the locations are drawn in Figure 2a. The simulated water level and discharge hydrographs of the proposed coupled model and the HEC-RAS model are drawn in Figure 3a–d for comparison. From these figures, the simulated results of the present coupled model all quite match the corresponding results of the HEC-RAS model despite some minor discrepancies in the water level hydrographs at the measured station P1. The NSE and MSE values for the water level and discharge hydrographs at the two measured stations are computed and displayed in Table 1. The water level peak and arrival time of the peak for the two models are displayed in Table 2. As Table 1 lists, the NSE values for the water level hydrograph of the two stations are, respectively, 0.956 and 0.863, and the NSE values for the water discharge hydrograph of the two stations are, respectively, 0.998 and 0.997. As for the MSE indicator, the values are 0.002 and <0.001 in the aspect of water level hydrograph and 0.142 and 0.105 in the aspect of water discharge hydrograph. Hence, based on the NSE and MSE indicators, the simulated hydrographs of the two models are quite similar. As to the results of the peak error analysis, the water level peaks for the coupled and HEC-RAS models are, respectively, 4.65 m and 4.76 m at the measured station P1 and, respectively, 4.04 m and 4.06 m at the measured station P2. From the viewpoint of the arrival times of peak, the values of the two models are, respectively, 167.0 min and 166.0 min at the measured station P1 and, respectively, 160.0 min and 160.0 min at the measured station P2. Based on the results of the peak error analysis, the maximum differences in the water level peak and arrival times between the two models are 9 cm and 1 min, respectively. Hence, based on the above results, the two models are found to provide quite similar simulated water level and discharge hydrographs, which also indicates that the two models provide similar predictions on the exchanged water volumes between their overland flow modeling and river flow modeling.

Table 1. The accuracy verification of the coupled model in the idealized study case by the NSE and MSE indicators for the water level and discharge hydrographs at the two measured stations. The simulated values of the HEC-RAS model are used as the exact solution for the computations of the NSE and MSE values.

Measured Station	The NSE Indicator		The MSE Indicator	
	Water Level	Water Discharge	Water Level	Water Discharge
P1	0.956	0.998	0.002	0.142
P2	0.863	0.997	<0.001	0.105

Table 2. The accuracy verification of the coupled model in the idealized study case through the peak error analysis. The water level peaks and arrival times of peak for the two models are displayed for comparison.

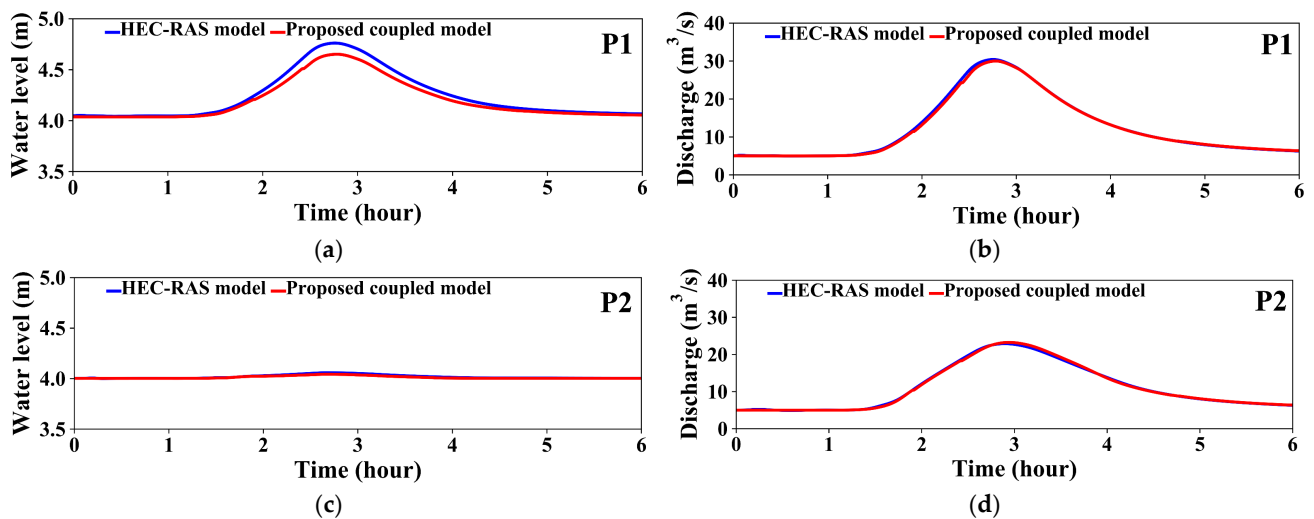| Measured Station	The HEC-RAS Model		The Coupled Model	
	Water Level Peak (m)	Arrival Time (min)	Water Level Peak (m)	Arrival Time (min)
P1	4.76	166.0	4.65	167.0
P2	4.06	160.0	4.04	160.0

Figure 3. The comparison of the water level and discharge hydrographs between the two models. (**a**) The simulated water level hydrographs and (**b**) the simulated water discharge hydrographs at the measured station P1. (**c**) The simulated water level hydrographs and (**d**) the simulated water discharge hydrographs at the measured station P2.

To confirm the above deduction, the discharge hydrographs from Floodplain A to the river of the two models and the overtopping discharge hydrographs from the river to Floodplain B are, respectively, displayed in Figure 4a,b for comparison. Inspection of the two figures reveals that the two models give almost identical predictions on the exchanged discharges despite some discrepancies in the overtopping discharge hydrographs. This phenomenon is due to the difference in the numerical scheme for simulating river flow, which is found to introduce some minor discrepancies in the water levels and discharges (Figure 3a–d). Also, the two models use different weir formulas for computing the exchanged water volume. Nevertheless, these differences are quite small and have minor influences on the flooding predictions in Floodplain B. The simulated flood extents in the two floodplains of the two models are drawn in Figure 5a,b, respectively. It can be confirmed that the two models provide almost the same predictions. Hence, based on the aforementioned results, the present coupled model is demonstrated to have almost the same accuracy as the HEC-RAS model in the aspects of the river flow and overland flow modeling. The developed linking methodology for coupling the 1D-RFM and 2D-OFM-CA is proven to be effective and correct.
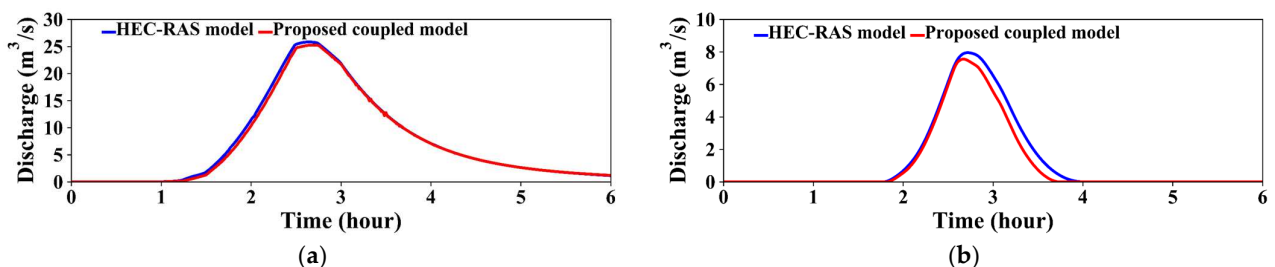

Figure 4. The comparison of the 1D–2D exchanged discharges between the HEC-RAS model and coupled model. (**a**) The discharge hydrographs from Floodplain A to the river. (**b**) The overtopping discharge hydrographs from the river to Floodplain B.
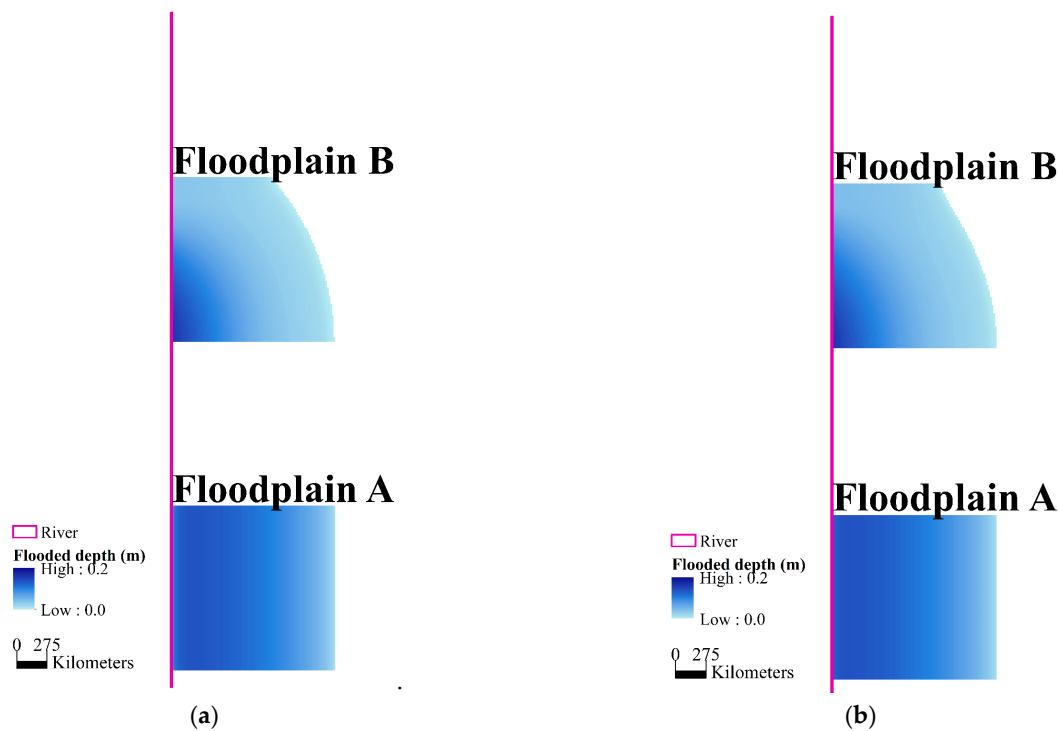
Figure 5. The simulated flood maps of (**a**) the coupled model and (**b**) the HEC-RAS model in the idealized study case, respectively.

As to the efficiency comparison, the total run times of the two models are recorded. For the present coupled model, it takes about 38 s to accomplish the simulation. From the viewpoint of the HEC-RAS model, it consumes 72 s. Consequently, the present coupled model is 47% faster than the HEC-RAS model. Given that the two models use almost the same technique for simulating 1D river flow and quite similar 1D-2D linking methodologies, the above efficiency enhancement is attributed to the 2D overland flow modeling. The 2D-OFM-CA in the coupled model delineates the water movement by using the water level as the key and computes the transported water volumes by the Manning and critical flow equations (Equations (9)–(16)). Additionally, the water level is used as the weight in the 2D-OFM-CA such that the 2D-OFM-CA only requires one operation of the Manning and critical flow equations to find the transported water volumes from a central cell to the four neighbor cells. Thus, in the 2D-OFM-CA, only simple algebraic equations are used to simulate water movement. Furthermore, the 2D-OFM-CA also includes the use of the update time step to further lower the computational demands in deciding the new adaptive time step. As for the 2D overland flow modeling in the HEC-RAS model, it uses the FVM to discretize the 2D shallow water equations, which involves tedious numerical operators for each term in the discretized 2D shallow water equations. Also, it finds the new adaptive time step at each time step. As a result, it is not surprising that the coupled model can be faster than the HEC-RAS model.

In summary, based on the above accuracy and efficiency comparison, the present coupled model is proven to provide almost the same accurate results but with obviously reduced computational times.

4. Model Applications

In this section, the proposed coupled model is applied to simulate basin-scale fluvial flooding on a real-scale and complex terrain to demonstrate its ability to efficiently and accurately conduct fluvial flooding assessment. It is noted that although it is better to use fluvial cases with experimental or observed data to verify the accuracy of the proposed coupled model, such fluvial cases are not available due to the lack of reliable experimen-

tal/observed data in overland flow modeling. Hence, the present study selects Test 7 (Upton-upon-Severn River and floodplain linkage) by the Environment Agency in the U.K. to verify the ability of the present 1D-2D model in large-scale fluvial assessment. The details of the adopted Test 7 are given as follows.

4.1. Study Site Delineation

The selected study site is a 20 km reach in the River Severn near Upton-upon-Severn with three floodplains around the reach. The extent of the study site is about 8 km long by 3 km wide, as Figure 6a depicts. The selected reach flows from north to south and consists of forty-two cross-sections from M013 to M054 with a total length of 19.02 km and an average bed slope of 0.000137. The width of the cross-sections ranges from 51 m (M045) to 128.6 m (M031). The digital elevation model (DEM) data are provided by the Environment Agency in the U.K. [6] with a very fine resolution of 1 m. Generally speaking, the terrain is steep at the western and eastern edges. The elevation is between 8.28 m and 16.00 m. As suggested by Néelz and Pender [6], the boundaries of the simulated 2D overland flows are approximately along the 16 m contour lines, as displayed in Figure 6a. There are three floodplains in this study site, as Figure 6a displays. For Floodplain 1, it is on the West bank of the river from the cross-sections M024 to M030. Floodplain 2 is located on the East bank of the river between the cross-sections M029 and M036. Floodplain 3 is on the West bank of the river in the range from halfway between the cross-sections M031 and M032 to halfway between the cross-sections M043 and M044. Finally, as drawn in Figure 6b, the selected reach has levees on the left and right banks to prevent overtopping water. The geometry and elevation data of these two banks are provided by Néelz and Pender [6] for the researcher to set up their 1D/2D linking.

As suggested by Néelz and Pender [6], the present study uses the 1 m-resolution Lidar DEM to create a DEM with a larger grid resolution for the rest simulations as the count of computational cells under the 1 m-resolution is too high. To introduce an appropriate count of the computational cells for the accuracy and efficiency comparison, the present study adopts a grid resolution of 10 m finer than the suggested grid resolution of Néelz and Pender [6] of 20 m. In the simulated area within the 16 m contour lines, there are 70,840 computational cells for the proposed coupled model and HRC-RAS model. The Manning roughness coefficient is given as 0.04 s/m$^{1/3}$ for all three floodplains. In the three floodplains, all boundaries are closed except for the edges linked to the river channel and other facilities such as culverts and sluices [6]. The locations and elevations of the two banks are used to set up the 1D-2D linking of the two models. It is worth mentioning that, for the proposed coupled model, a river cell that has no other connected computational cells will not be marked as the river cell to avoid the situation that the water is trapped in this river cell. Also, in the two models, the assigned embankment elevation for a computational cell with a passerby embankment should be the maximum value between the derived embankment elevation from data of Néelz and Pender [6] and the bed elevation of the computational cell. Initially, the three floodplains are completely dry. As to the settings in the river, the bridge at the north end of Upton (in between the cross-sections M033 and M034) is ignored. Also, in river segments where there are no connected floodplains along the corresponding banks, a glass wall approach is applied such that the river will not spill out water. A uniform Manning roughness coefficient of 0.028 s/m$^{1/3}$ is applied to the river. At the upstream cross-section M013, an inflow discharge series drawn in Figure 6c is prescribed. For the downstream boundary condition in the river, a rating curve (flow versus head, displayed in Figure 6d) is applied at the cross-section M054. Initially, a uniform water level of 9.8 m is applied to the river. The simulation duration is 72 h. The coupled and HEC-RAS models are built according to the suggestions of their manuals. It is worth mentioning that, in analogy to the idealized case in the previous section, the model parameters of the coupled model are assigned with the suggested values of the manual [29] for the purpose of demonstration. As for the HEC-RAS model, almost all cells

are delineated as 10 m square cells except for the cells adjacent to the riverbank lines. The corresponding simulations are conducted on the same PC as in the previous section.
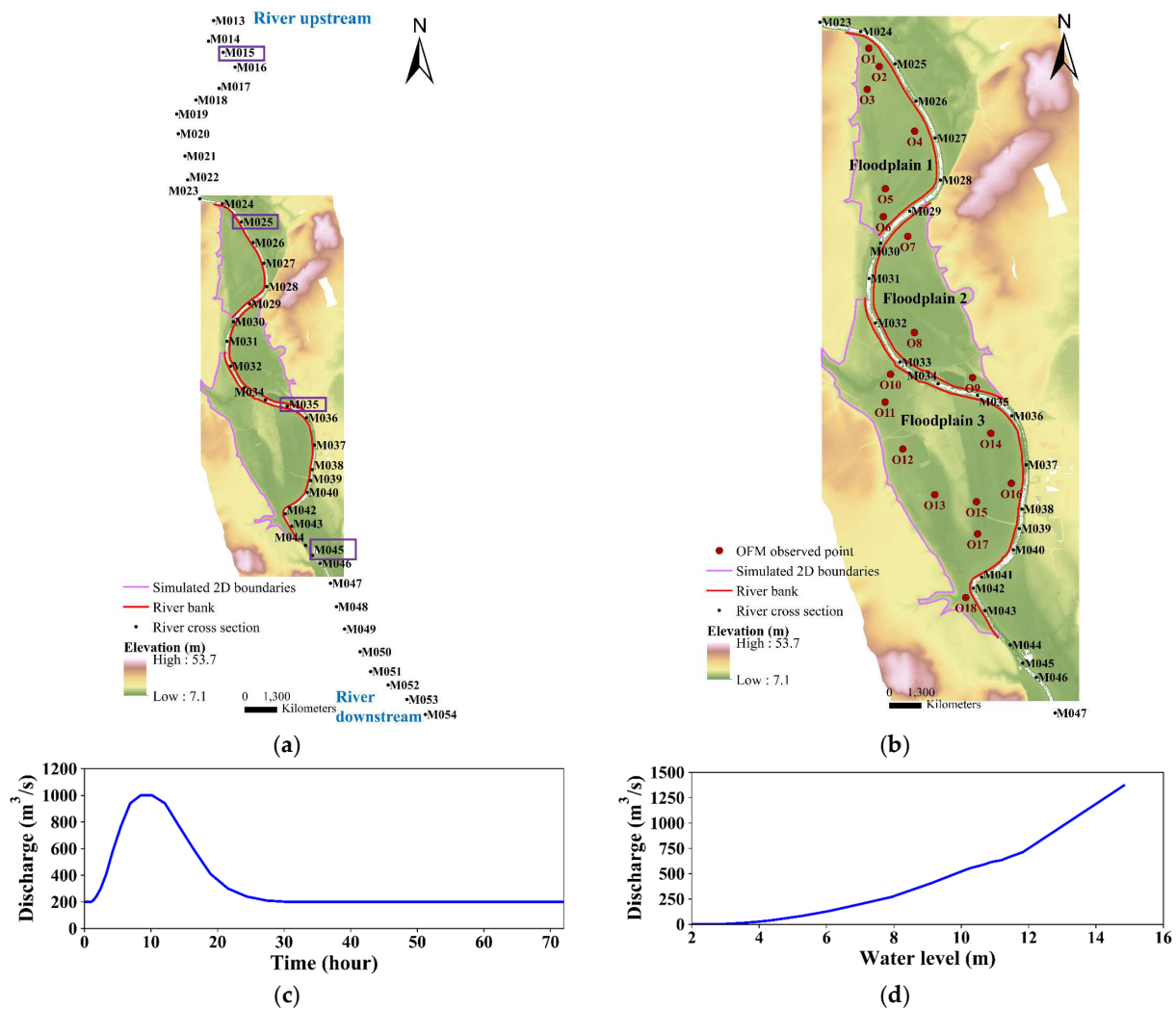

Figure 6. The real-scale study case in the Severn River basin. (**a**) The map of the modeled reach of the River Severn and the three floodplains. The digital elevation model, locations of the forty-two cross-sections, three floodplains, and 16 m contour lines for defining the simulated boundaries of overland flow modeling are plotted for illustration. The four cross-sections for accuracy comparison (i.e., M015, M025, M035, and M045) are highlighted with four purple rectangles. The upstream and downstream sides of the river are also marked. (**b**) The locations of the left and right banks along the river and eighteen observed points for accuracy comparison in the overland flow modeling. (**c**) The inflow discharge series at the upstream start of the modeled river. (**d**) The rating curve prescribed as the boundary condition at the downstream end of the modeled river.

The comparison of the two models is conducted by inspecting the water level hydrographs at the four cross-sections (i.e., M015, M025, M035, and M045, locations can be found in Figure 6a), and the water level hydrographs at the eighteen observed points in the three floodplains (locations are displayed in Figure 6b). Nevertheless, due to space limitation, in analogy to Néelz and Pender [6], the present study picks up nine observed points among these eighteen observed points for the comparison, i.e., the observed points O1, O2, and O6 in Floodplain 1, O8 and O9 in Floodplain 2, and O11, O12, O14, and O17 in Floodplain 3. To quantify the accuracy of the proposed coupled model, similar to the idealized study case, the NSE and MSE values for the water level hydrograph in the river and floodplains are computed by taking the results of the HEC-RAS model as the exact solutions. In addition,

the peak error analysis is performed to discover the similarity between the two models. The results are next discussed.

4.2. Accuracy Evaluation and Efficiency Assessment

The simulated water level hydrographs at the four cross-sections (M015, M025, M035, and M045) of the two models are drawn in Figure 7a–d for comparison. From these four figures, the results of the coupled model are found to match the results of the HEC-RAS model well. Such a consistency can also be observed from the values of the NSE and MSE indicators at the four cross-sections (i.e., M015, M025, M035, and M045), as displayed in Table 3 for inspection. From Table 3, the NSE values for the four cross-sections are 0.994, 0.991, 0.993, and 0.994, respectively, and the MSE values for the four cross-sections are 0.021, 0.024, 0.013, and 0.018, respectively, which indicates that the water level hydrographs between the two models are quite similar. However, as already displayed in Figure 7a–d, the coupled model tends to overestimate the water level peaks and arrival times at the M015, M025, and M035 cross-sections, as can be seen in Table 4. As for the M045 cross-section, the water level peak is underestimated but the arrival time is still overestimated like the other three cross-sections. Nevertheless, it is found that the difference in the water level peak between the coupled model and the HEC-RAS model is small (with a maximum difference of up to 0.2 m) even though the coupled model overestimates the arrival time at all four cross-sections. The water level hydrographs at the nine observed points are drawn in Figure 8a–i for assessment. Generally speaking, the coupled model predicts similar results in both the rising and falling limbs compared to the HEC-RAS model in all nine observed points. Nevertheless, the arrival times of peaks are found to be delayed in all nine water level hydrographs. Also, the water level peaks are overestimated at the observed points O1 and O2 and underestimated at the rest seven points (O6, O8, O9, O11, O12, O14, and O17). The NSE and MSE values at these nine observed points are listed in Table 5 for comparison. Overall, the water level hydrographs between the two models are satisfactorily similar except for the observed point O11 where a relatively low NSE value and a relatively high MSE value are found. The results of the peak error analysis on these nine observed points are displayed in Table 6. From this table, it is seen that the arrival times are delayed in almost all observed points (with a maximum of up to 1.62 h at the observed point O6). On the other hand, in terms of the water level peaks, the difference between the coupled model and the HEC-RAS model is small (with a maximum of up to 0.37 m at the observed point O1). Also, the observed points O1 and O2 are found to have relatively larger water level peak errors than the other observed points. Nevertheless, the differences in the water level peak and arrival time are acceptably small. The simulated flooded extents of the two models are displayed in Figure 9a,b. Inspection of these two figures reveals that the coupled model predicts a similar flood extent as the HEC-RAS model. Thus, based on the above results, the coupled model is demonstrated to give satisfactorily similar results compared to the HEC-RAS model.

Table 3. The accuracy evaluation of the coupled model in the basin-scale study case by the NSE and MSE indicators for the water level hydrographs at the four cross-sections M015, M025, M035, and M045 in the river. The simulated values of the HEC-RAS model are used as the exact solution for the computations of the NSE and MSE values.

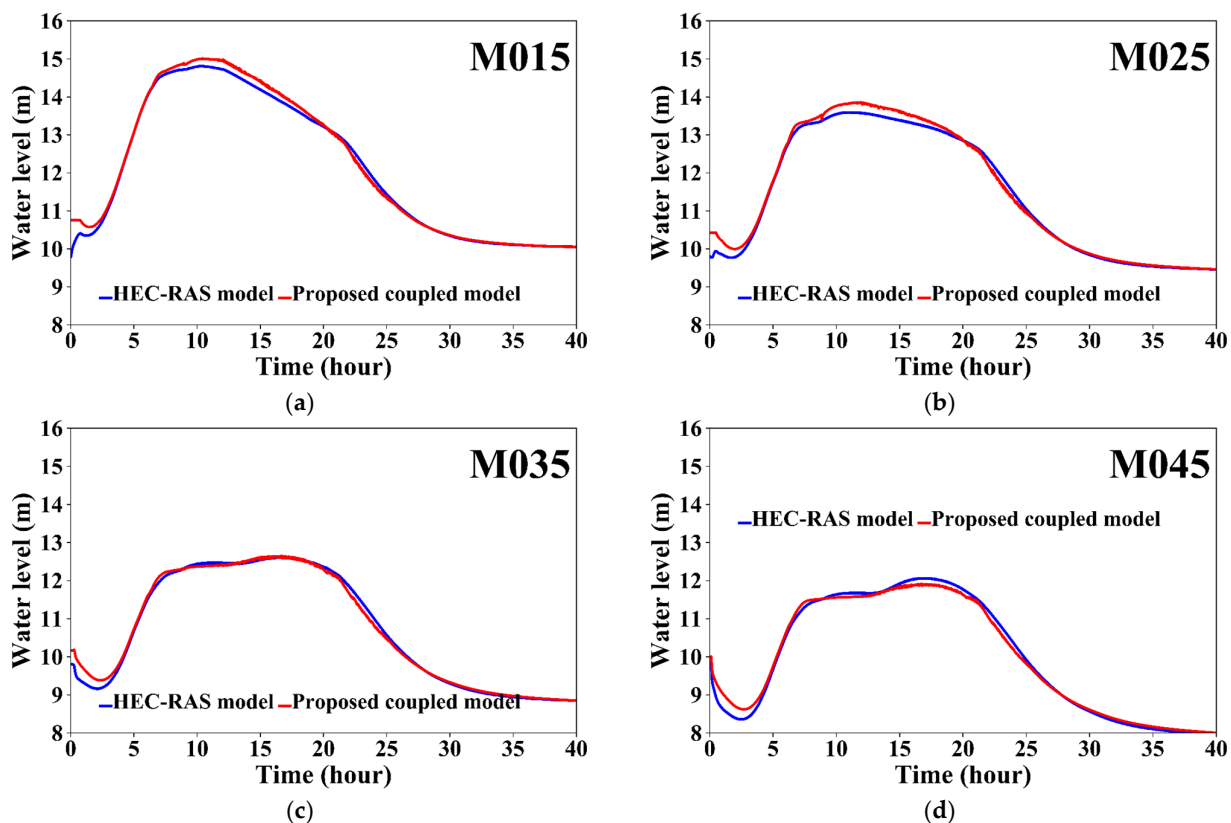| Cross-Section	The NSE Indicator	The MSE Indicator
M015	0.994	0.021
M025	0.991	0.024
M035	0.994	0.013
M045	0.993	0.018

Figure 7. The simulated water level hydrographs of the cross-sections (**a**) M015, (**b**) M025, (**c**) M035, and (**d**) M045, respectively, of the two models in the basin-scale study case.

Table 4. The accuracy evaluation of the coupled model in the basin-scale study case by the peak error analysis at the four cross-sections in the river.

Cross-Section	The HEC-RAS Model		The Coupled Model	
	Water Level Peak (m)	Arrival Time (h)	Water Level Peak (m)	Arrival Time (h)
M015	14.81	10.13	15.01	10.42
M025	13.59	10.62	13.86	11.90
M035	12.61	16.35	12.65	16.67
M045	12.06	16.45	11.92	16.75

Table 5. The accuracy evaluation of the coupled model in the basin-scale study case by the NSE and MSE indicators for the water level hydrographs at the nine observed points. The simulated values of the HEC-RAS model are used as the exact solution.

Observed Point	The NSE Indicator	The MSE Indicator
O1	0.943	0.029
O2	0.928	0.053
O6	0.978	0.015
O8	0.976	0.025
O9	0.952	0.031
O11	0.818	0.074
O12	0.914	0.011
O14	0.982	0.011
O17	0.990	0.008

Figure 8. The simulated water level hydrographs at the observed points (**a**) O1, (**b**) O2, (**c**) O6, (**d**) O8, (**e**) O9, (**f**) O11, (**g**) O12, (**h**) O14, and (**i**) O17, respectively, in the basin-scale study case.

Table 6. The accuracy evaluation of the coupled model by the peak error analysis at the nine observed points in the floodplains. The water level peaks and arrival times of peak for the two models are displayed for evaluation.

Observed Point	The HEC-RAS Model		The Coupled Model	
	Water Level Peak (m)	Arrival Time (h)	Water Level Peak (m)	Arrival Time (h)
O1	13.57	10.95	13.94	11.93
O2	13.53	11.07	13.89	11.92
O6	13.47	11.10	13.30	12.72
O8	12.80	15.62	12.93	15.68
O9	12.74	15.53	12.75	16.20
O11	12.74	15.77	12.77	16.88
O12	12.43	16.87	12.32	17.45
O14	12.52	16.88	12.52	16.37
O17	12.43	16.95	12.25	17.45

The aforementioned discrepancies between the two models are majorly attributed to the difference in the computing methodology of the OFM between the two models. As previously found by Guidolin et al. [40], compared to a dynamic-wave model, the 2D-OFM-CA tends to slightly underestimate the moving speeds of the overland flows due to the lack of an inertia effect. Consequently, for the observed points that are close to the embankments where the river overtops (i.e., O1 and O2), the water level peaks and arrival times are both overestimated. For the other seven observed points, as they are located at the relatively downstream side of the surface runoffs, the arrival times are subsequently

underestimated by the underestimation of the moving speeds of the overland flows. This kind of phenomenon also subsequently prolongs the overtopping process and makes the water levels in the river become higher as the overtopped water cannot be sent to the 2D OFM due to the high water levels in the river cells. Thus, the overtopped water volume and subsequent overland flow volume, as well as the lateral surface water volume, are both relatively underestimated. Nevertheless, the differences in the river (Figure 7a and Tables 3 and 4) and overland (Figure 8a–i, Figure 9a,b, and Tables 5 and 6) are acceptably small. Thus, the coupled model can reach almost the same accuracy as the HEC-RAS model.

Finally, in terms of efficiency, the total run times of the two models are recorded and compared. The present coupled model and HEC-RAS model, respectively, take about 1.27 h and 2.15 h to accomplish their simulations. Hence, the coupled model is 41% faster than the HEC-RAS model in this basin-scale study case, which demonstrates the effectiveness of using an efficient 2D-OFM-CA instead of the 2D overland flow modeling in the HEC-RAS model. Also, it can be deduced that the given parameters for the 2D-OFM-CA can lead to quite efficient simulation with acceptable accuracy. Nevertheless, it is worth mentioning that such an efficiency enhancement of the 2D-OFM-CA is attributed to the fact that the terrain of the three floodplains is not completely flat, and the flow conditions of the overland flows in the three floodplains are regular flows in a large time duration. When the terrain becomes completely flat or flow conditions are dominated by strong discontinuous flows over a large time duration, the efficiency of the coupled model will decrease because of the lack of an inertia effect in the 2D-OFM-CA, as already discussed by Guidolin et al. [40] and Chang et al. [24]. In summary, the coupled model is demonstrated to reach almost the same accuracy as the HEC-RAS model with noticeably reduced computation times. The proposed coupled model only requires 59% run times of the HEC-RAS model to accomplish the simulation.
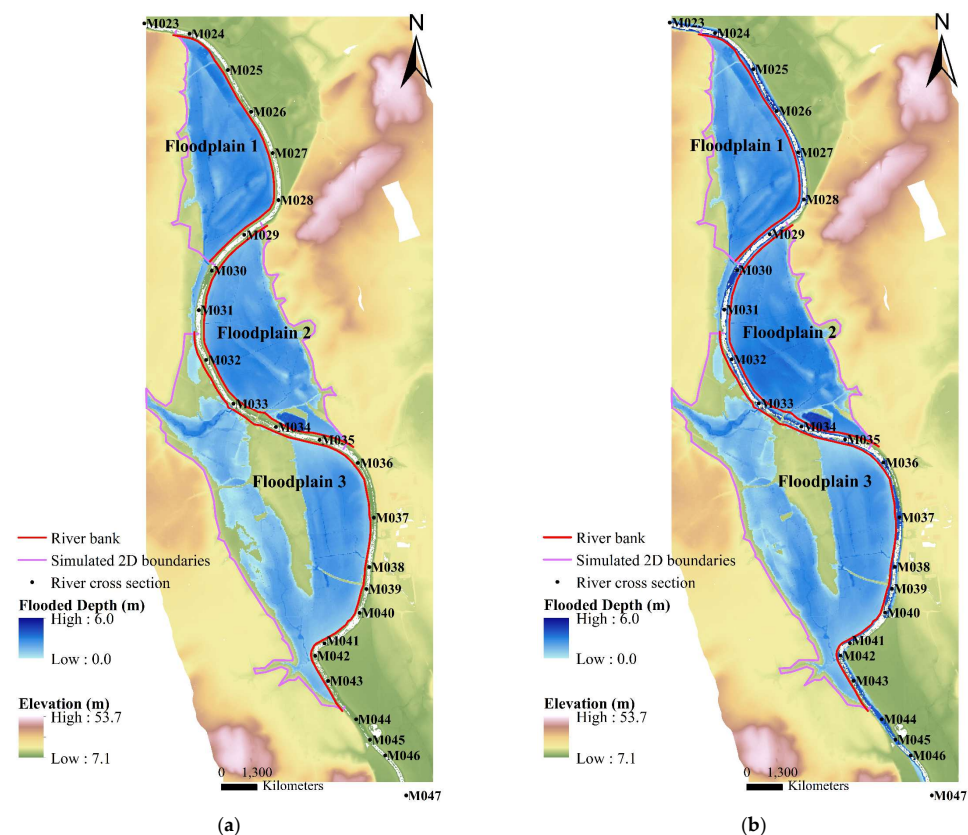

Figure 9. The simulated flood extents of the (**a**) coupled model and (**b**) HEC-RAS model, respectively, in the basin-scale study case.

5. Conclusions

The present study proposes a new coupled river–overland (1D-2D) modeling that comprises a widely-used CA-based urban inundation modeling (2D-OFM-CA) and a 1D unsteady river flow modeling (1D-RFM). Bidirectional interaction between the 1D-RFM and 2D-OFM-CA is taken along river embankments in the coupled model. Rules are incorporated to handle the corresponding geometric linking, and the subsequent exchanged water volume is computed by the free and submerged weir formulas. The ability of the coupled model in fluvial flood modeling is assessed and compared with the commercial software (HEC-RAS model version 5.0.7) through an idealized fluvial case and an extensively studied real-scale fluvial case in the Severn River Basin. Based on the simulated results, the following conclusions are drawn.

Overall, in terms of numerical accuracy, the coupled model is found to have almost the same accuracy as the HEC-RAS model in both river flow and overland flow modeling in the two study cases, which also demonstrates the correctness of the linking methodology between the 1D-RFM and 2D-OFM-CA. As to the numerical efficiency, the coupled model is found to be 47% and 41% faster than the HEC-RAS model in the two study cases, respectively. Thus, the coupled model is demonstrated to be as accurate as the HEC-RAS model, with a noticeable reduction in computational time. In summary, the proposed coupled model is proven to have considerable potential to be an effective alternative for fluvial flooding in the river basin.

Author Contributions: Conceptualization, H.-L.Y., C.-H.W. and S.-Y.M.; methodology, H.-L.Y. and S.-Y.M.; software, H.-L.Y. and S.-Y.M.; validation, H.-L.Y. and S.-Y.M.; formal analysis, H.-L.Y., C.-H.W. and T.-J.C.; investigation, H.-L.Y., C.-H.W. and S.-Y.M.; resources, C.-H.W. and S.-Y.M.; data curation, S.-Y.M. and H.-L.Y.; writing—original draft preparation, H.-L.Y. and S.-Y.M.; writing—review and editing, H.-L.Y. and T.-J.C.; visualization, H.-L.Y. and S.-Y.M.; supervision, T.-J.C.; project administration, T.-J.C.; funding acquisition, T.-J.C. All authors have read and agreed to the published version of the manuscript.

Data Availability Statement: The data presented in this study are available on request from the corresponding author.

Conflicts of Interest: The authors declare no conflicts of interest.

References

1. Castro-Orgaz, O.; Hager, W.H. *Shallow Water Hydraulics*; Springer: Cham, Switzerland, 2019.
2. Verwey, A. Latest development in floodplain modelling-1D/2D integration. In Proceedings of the Australian Conference on Hydraulics in Civil Engineering, the Institute of Engineers, Hobart, Australia, 20–30 November 2001; pp. 13–24.
3. Lin, B.; Wicks, J.M.; Falconer, R.A.; Adams, K. Integrating 1D and 2D hydrodynamic models for flood simulation. *Proc. Inst. Civ. Eng.-Water Manag.* **2006**, *159*, 19–25. [CrossRef]
4. Kuiry, S.N.; Sen, D.; Bates, P.D. Coupled 1D-quasi 2D flood inundation model with unstructured grids. *J. Hydraul. Eng.* **2010**, *136*, 493–506. [CrossRef]
5. Masoero, A.; Claps, P.; Asselman, N.E.M.; Mosselman, E.; Di Baldassarre, G. Reconstruction and analysis of the Po River inundation of 1951. *Hydrol. Process.* **2013**, *27*, 1341–1348. [CrossRef]
6. Néelz, S.; Pender, G. *Benchmarking the Latest Generation of 2D Hydraulic Modelling Packages*; U.K. Environment Agency: Bristol, UK, 2013.
7. Liang, D.; Falconer, R.A.; Lin, B. Linking one- and two-dimensional models for free surface flows. *Water Manag.* **2007**, *160*, 145–151. [CrossRef]
8. Morales-Hernánez, M.; Petacciab, G.; Brufaua, P.; García-Navarroa, P. Conservative 1D-2D coupled numerical strategies applied to river flooding: The Tiber (Rome). *Appl. Math. Model.* **2016**, *40*, 2087–2105. [CrossRef]
9. Liu, Q.; Qin, Y.; Zhang, Y.; Li, Z. A coupled 1D-2D hydrodynamic model for flood simulation in flood detention basin. *Nat. Hazards* **2015**, *75*, 1303–1325. [CrossRef]

10. Brunner, G.W. *HEC-RAS River Analysis System, Hydraulic Reference Manual*; U.S. Army Corps of Engineers Institute for Water Resources Hydrologic Engineering Center: Washington, DC, USA, 2016.

11. Innovyze. *Inforwork ICM Help, version v3.0*; Innovyze: Portland, OR, USA, 2012.

12. Hénonin, J.; Ma, H.; Yang, Z.Y.; Hartnack, J.; HavnØ, K.; Gourbesville, P.; Mark, O. Citywide multi-grid urban flood modelling: The July 2012 flood in Beijing. *Urban Water J.* **2013**, *12*, 52–66. [CrossRef]

13. Chaudhry, M.H. *Open-Channel Flow*, 3rd ed.; Springer: New York, NY, USA, 2022.

14. Lee, M.E.; Seo, I.W. Analysis of pollutant transport in the Han River with tidal current using a 2D finite element model. *J. Hydro-Environ. Res.* **2007**, *1*, 30–42. [CrossRef]

15. Bates, P.D.; Horritt, M.S.; Fewtrell, T.J. A simple inertia formulation of the shallow water equations for efficient two-dimensional flood inundation modeling. *J. Hydrol.* **2010**, *387*, 33–45. [CrossRef]

16. Kao, H.M.; Chang, T.J. Numerical modeling of dambreak-induced flood and inundation using smoothed particle hydrodynamics. *J. Hydrol.* **2012**, *448–449*, 232–244. [CrossRef]

17. Chang, T.J.; Wang, C.H.; Chen, A.S. A novel approach to model dynamic flow interactions between storm sewer system and overland surface for different land covers in urban areas. *J. Hydrol.* **2015**, *524*, 662–679. [CrossRef]

18. Ferrari, A.; Vacondio, R.; Dazzi, S.; Mignosa, P. A 1D-2D Shallow Water Equations solver for discontinuous porosity field based on a Generalized Riemann Problem. *Adv. Water Resour.* **2017**, *107*, 233–249. [CrossRef]

19. Martins, R.; Leandro, J.; Djordjević, S. Wetting and drying numerical treatments for the Roe Riemann scheme. *J. Hydraul. Res.* **2018**, *56*, 256–267. [CrossRef]

20. Yu, H.L.; Chang, T.J. A hybrid shallow water solver for overland flow modelling in rural and urban areas. *J. Hydrol.* **2021**, *598*, 126262. [CrossRef]

21. Zhao, J.; Liang, Q. Novel variable reconstruction and friction term discretization schemes for hydrodynamic modelling of overland flow and surface water flooding. *Adv. Water Resour.* **2022**, *163*, 104187. [CrossRef]

22. Xia, X.; Liang, Q.; Ming, X.; Hou, J. An efficient and stable hydrodynamic model with novel source term discretization schemes for overland flow and flood simulations. *Water Resour. Res.* **2017**, *53*, 3730–3759. [CrossRef]

23. Muthusamy, M.; Casado, M.R.; Butler, D.; Leinster, P. Understanding the effects of Digital Elevation Model resolution in urban fluvial flood modelling. *J. Hydrol.* **2021**, *596*, 126088. [CrossRef]

24. Chang, T.J.; Yu, H.L.; Wang, C.H.; Chen, A.S. Dynamic-wave cellular automata framework for shallow water flow modeling. *J. Hydrol.* **2022**, *613*, 128449. [CrossRef]

25. Jamali, B.; Löwe, R.; Bach, P.M.; Urich, C.; Arnbjerg-Nielsen, K.; Deletic, A. A rapid urban flood inundation and damage assessment model. *J. Hydrol.* **2018**, *564*, 1085–1098. [CrossRef]

26. Savage, J.T.S.; Bates, P.; Freer, J.; Neal, J.; Aronica, G. When does spatial resolution become spurious in probabilistic flood inundation predictions? *Hydrol. Process.* **2016**, *30*, 2014–2032. [CrossRef]

27. Vacondio, R.; Dal Palù, A.; Mignosa, P. GPU-enhanced finite volume shallow water solver for fast flood simulations. *Environ. Modell. Softw.* **2014**, *57*, 60–75. [CrossRef]

28. Leandro, J.; Chen, A.S.; Schumann, A. A 2D parallel diffusive wave model for floodplain inundation with variable time step (P-DWave). *J. Hydrol.* **2014**, *517*, 250–259. [CrossRef]

29. Caviedes-Voullième, D.; Fernández-Pato, J.; Hinz, C. Performance assessment of 2D zero-inertia and shallow water models for simulating rainfall-runoff process. *J. Hydrol.* **2020**, *584*, 124663. [CrossRef]

30. Krupka, M. A Rapid Inundation Flood Cell Model for Flood Risk Analysis. Ph.D. Thesis, Heriot-Watt University, Edinburgh, Scotland, 2009.

31. Bernini, A.; Franchini, M. A rapid model for delimiting flooded areas. *Water Resour. Manag.* **2013**, *27*, 3825–3846. [CrossRef]

32. Maksimović, Č.; Prodanovic, D.; Boonya-aroonnet, S.; Leitão, J.P.; Djordjević, S.; Allitt, R. Overland flow and pathway analysis for modelling of urban pluvial flooding. *J. Hydraul. Res.* **2009**, *47*, 512–523. [CrossRef]

33. Chopard, B. Cellular automata modeling of physical systems. In *Encyclopedia of Complexity and Systems Science*, 1st ed.; Meyers, R.A., Ed.; Springer: New York, NY, USA, 2009; pp. 856–892.

34. Hadeler, K.P.; Müller, J. *Cellular Automata: Analysis and Applications*; Springer: Cham, Switzerland, 2017.

35. Wolfram, S. Cellular automata as models of complexity. *Nature* **1984**, *311*, 419–424. [CrossRef]

36. Yu, H.L.; Chang, T.J. Modeling particulate matter concentration in indoor environment with cellular automata framework. *Build Environ.* **2022**, *214*, 108898. [CrossRef]

37. Dottori, F.; Todini, E. Developments of a flood inundation model based on the cellular automata approach: Testing different methods to improve model performance. *Phys. Chem. Earth Parts ABC* **2011**, *36*, 266–280. [CrossRef]

38. Ghimire, B.; Chen, A.S.; Guidolin, M.; Keedwell, E.C.; Djordjević, S.; Savić, D.A. Formulation of a fast 2D urban pluvial flood model using a cellular automata approach. *J. Hydroinform.* **2013**, *15*, 676. [CrossRef]

39. Cai, X.; Li, Y.; Wen, G.X.; Wu, W. Mathematical model for flood routing based on cellular automation. *Water Sci. Eng.* **2014**, *7*, 133–142.

40. Guidolin, M.; Chen, A.S.; Ghimire, B.; Keedwell, E.C.; Djordjević, S.; Savić, D.A. A weighted cellular automata 2D inundation model for rapid flood analysis. *Environ. Model. Softw.* **2016**, *84*, 378–394. [CrossRef]

41. Jahanbazi, M.; Özgen, I.; Aleixo, R.; Hinkelmann, R. Development of a diffusive wave shallow water model with a novel stability condition and other new features. *J. Hydroinform.* **2017**, *19*, 405–425. [CrossRef]

42. Jamali, B.; Bach, P.M.; Cunningham, L.; Deletic, A. A cellular automata fast flood evaluation (CA-ffé) model. *Water Resour. Res.* **2019**, *55*, 4936–4953. [CrossRef]

43. Tavakolifar, H.; Abbasizadeh, H.; Nazif, S.; Shahghasemi, E. Development of 1D-2D urban flood simulation model based on modified cellular automata approach. *J. Hydrol. Eng.* **2020**, *26*, 2. [CrossRef]

44. Caviedes-Voullième, D.; Fernández-Pato, J.; Hinz, C. Cellular automata and finite volume solvers converge for 2D shallow flow modeling for hydrological modelling. *J. Hydrol.* **2018**, *563*, 411–417. [CrossRef]

45. Yin, D.; Evans, B.; Wang, Q.; Chen, Z.; Jia, H.; Chen, A.S.; Fu, G.; Ahmad, S.; Leng, L. Integrated 1D and 2D model for better assessing runoff quantity control of low impact development facilities on community scale. *Sci. Total Environ.* **2020**, *720*, 137630. [CrossRef] [PubMed]

46. Chang, T.J.; Yu, H.L.; Wang, C.H.; Chen, A.S. Overland-gully-sewer (2D-1D-1D) urban inundation modeling based on cellular automata framework. *J. Hydrol.* **2021**, *603*, 127001. [CrossRef]

47. Hsu, M.H.; Lin, S.H.; Fu, J.C.; Chung, S.F.; Chen, A.S. Longitudinal stage profiles forecasting in rivers for flash floods. *J. Hydrol.* **2010**, *388*, 426–437. [CrossRef]

48. Hunter, N.M.; Horritt, M.S.; Bates, P.D.; Wilson, M.D.; Wener, M.G.F. An adaptive time step solution for raster-based storage cell modelling of floodplain inundation. *Adv. Water Resour.* **2005**, *28*, 975–991. [CrossRef]

49. Casulli, V. A high-resolution wetting and drying algorithm for free-surface hydrodynamics. *Int. J. Numer. Meth. Fl.* **2008**, *60*, 391–408. [CrossRef]

50. Nash, J.E.; Sutcliffe, J.V. River flow forecasting through conceptual models part I—A discussion of principles. *J. Hydrol.* **1970**, *10*, 282–290. [CrossRef]